Journal of Materials Chemistry C

ROYAL SOCIETY OF CHEMISTRY

PAPER

Cite this: J. Mater. Chem. C, 2020, 8, 12677

Bandgap and strain engineering in epitaxial rocksalt structure $(Ti_{0.5}Mg_{0.5})_{1-x}Al_xN(001)$ semiconductors†

Baiwei Wang,[a] Minghua Zhang,[a] Vijaya Adhikari,[b] Peijiao Fang,[a] Sanjay V. Khare[b] and Daniel Gall *[a]

Rocksalt structure nitrides emerge as a promising class of semiconductors for high-temperature thermoelectric and plasmonic applications. Controlling the bandgap and strain is essential for the development of a wide variety of electronic devices. Here we use $(Ti_{0.5}Mg_{0.5})_{1-x}Al_xN$ as a model system to explore and demonstrate the tunability of both the bandgap and the strain state in rocksalt structure nitrides, employing a combined experimental and computational approach. $(Ti_{0.5}Mg_{0.5})_{1-x}Al_xN$ layers with $x \leq 0.44$ deposited on MgO(001) substrates by reactive co-sputtering at 700 °C are epitaxial single crystals with a solid-solution B1 rocksalt structure. The lattice mismatch with the substrate decreases with increasing x, leading to a transition in the strain-state from partially relaxed (74% and 38% for $x = 0$ and 0.09) to fully strained for $x \geq 0.22$. First-principles calculations employing 64-atom Special Quasirandom Structures (SQS) indicate that the lattice constant decreases linearly with x according to $a = (4.308 - 0.234x)$ Å for $0 \leq x \leq 1$. In contrast, the measured relaxed lattice parameter $a_o = (4.269 - 0.131x)$ Å is linear only for $x \leq 0.33$, its composition dependence is less pronounced, and $x > 0.44$ leads to the nucleation of secondary phases. The fundamental (indirect) bandgap predicted using the same SQS supercells and the HSE06 functional increases from 1.0 to 2.6 eV for $x = 0$–0.75. In contrast, the onset of the measured optical absorption due to interband transitions increases only from 2.3 to 2.6 eV for $x = 0$–0.44, suggesting that the addition of Al in the solid solution relaxes the electron momentum conservation and causes a shift from direct to indirect gap transitions. The resistivity increases from 9.0 to 708 μΩ m at 77 K and from 6.8 to 89 μΩ m at 295 K with increasing $x = 0$–0.44, indicating an increasing carrier localization associated with a randomization of cation site occupation and the increasing bandgap which also causes a 33% reduction in the optical carrier concentration. The overall results demonstrate bandgap and strain engineering in rocksalt nitride semiconductors and show that, in contrast to conventional covalent semiconductors, the random cation site occupation strongly affects optical transitions.

Received 29th July 2020,
Accepted 18th August 2020

DOI: 10.1039/d0tc03598j

rsc.li/materials-c

Introduction

Nitride semiconductors with a rocksalt crystal structure are relatively unexplored but are expected to exhibit the advantageous physical properties known from conductive cubic transition metal nitrides which have a high hardness, chemical inertness, and high temperature stability and are used as hard wear-protective layers, diffusion barriers in microelectronics and photovoltaics, and optical or decorative coatings.[1–8] Correspondingly, semiconducting rocksalt structure nitrides have promise for semiconducting devices in harsh, high-temperature environments but have also attracted interest because of their potential use in thermoelectric,[9–11] plasmonic,[12–14] and solar energy harvesting[15–18] devices. Rocksalt structure nitrides are semiconductors if they have only 8 valence electrons per formula unit which completely fill the hybridized N_2p-Metal_d valence band while leaving the d conduction band empty.[19] ScN is the prototypical rocksalt structure refractory nitride semiconductor with an indirect fundamental bandgap of 0.92 ± 0.05 eV.[20] Incorporating Al to form $Sc_{1-x}Al_xN$ ternary solid solutions allows to tune the bandgap as well as the electrical and thermal conductivity.[21–23] However, ScN and related alloys have practical challenges associated with the high cost and limited purity of the Sc source metal[20] and

[a] Department of Materials Science and Engineering, Rensselaer Polytechnic Institute, Troy, NY 12180, USA. E-mail: galld@rpi.edu
[b] Department of Physics and Astronomy, University of Toledo, 2801 West Bancroft Street, Toledo, OH 43606, USA

† Electronic supplementary information (ESI) available: Optical reflection spectra for all samples in this study, which are used to determine the optical color of each sample (PDF). See DOI: 10.1039/d0tc03598j

limited crystalline quality due to a relatively large lattice misfit with MgO substrates.[21] An alternative promising option to form rocksalt structure nitride semiconductors is to alloy MeN (Me = Ti, Zr, and Hf) with alkaline earth elements such as Mg,[19,24,25] as simple electron counting suggests that a 50–50 Me-to-alkaline-earth ratio leads to a vanishing carrier density, while $x < 0.5$ and $x > 0.5$ in $Me_{1-x}Mg_xN$ correspondingly result in n and p-type electron transport.[9,10,16] Reported optical measurements and photoelectron spectroscopy studies confirm that $Ti_{0.5}Mg_{0.5}N$, for example, is a semiconductor with an optical bandgap of 2.0–2.2 eV.[24,26,27]

Introducing Al in transition-metal nitrides is common as it is known to improve the mechanical strength and electrochemical stability.[28,29] In addition, we envision that alloying $Ti_{0.5}Mg_{0.5}N$ with AlN is particularly promising from a perspective of new rocksalt structure semiconductors: (1) Al incorporation provides opportunities for bandgap engineering as the gap in $(Ti_{0.5}Mg_{0.5})_{1-x}Al_xN$ alloys is expected to increase with x and relaxation of the momentum conservation may facilitate optical transitions at the fundamental indirect gap. (ii) The Al introduction may reduce the point defect density in $Ti_{0.5}Mg_{0.5}N$.[30] In particular, $Ti_{1-x}Mg_xN$ alloys contain a considerable density of nitrogen vacancies[26,31] caused by a decreasing formation energy with increasing Mg content.[19] We expect that Al counteracts the vacancy formation because an increasing x in $(Ti_{0.5}Mg_{0.5})_{1-x}Al_xN$ increases the bandgap and effectively reduces the fraction of cation sites occupied by Mg, likely leading to an increase in the nitrogen vacancy formation energy. (iii) Al in $(Ti_{0.5}Mg_{0.5})_{1-x}Al_xN$ alloys is expected to reduce the lattice mismatch with MgO substrates and, therefore, suppress associated misfit strain and dislocations. The corresponding increase in crystalline quality is useful towards exploring semiconducting properties of rocksalt structure nitrides.

In this paper, we report on the growth and properties of epitaxial $(Ti_{0.5}Mg_{0.5})_{1-x}Al_xN(001)$ layers ($0.00 \leq x \leq 0.44$) on MgO(001) substrates by reactive magnetron co-sputtering from titanium, magnesium and aluminum targets in 5 mTorr pure N_2 at 700 °C. X-ray diffraction ω–2θ scans, ω-rocking curves, and reciprocal space maps show that solid-solution B1 rocksalt $(Ti_{0.5}Mg_{0.5})_{1-x}Al_xN$ layers with $0 \leq x \leq 0.44$ are epitaxial single crystals, while extra peaks from a secondary phase emerge for layers with a higher Al content. The lattice constant decreases with increasing x, leading to a decreasing lattice mismatch and, in turn, an increasing crystalline quality, a decreasing degree of strain relaxation, and layers that are fully coherent with the substrate for $x \geq 0.22$. Optical analyses show that increasing x results in an increasing bandgap and a decreasing carrier concentration, while electron transport measurements indicate an increasing resistivity and carrier localization. Complementary first-principles simulations corroborate the increasing bandgap and the decreasing lattice parameter with increasing x. The overall results confirm the envisioned potential for strain and bandgap engineering in rocksalt structure nitride semiconductors.

Methods

$(Ti_{0.5}Mg_{0.5})_{1-x}Al_xN$ layers were deposited by reactive magnetron co-sputtering in a load-locked ultra-high vacuum deposition system that is well suited to deposit epitaxial nitride layers with negligible oxygen contamination.[32,33] Double-side polished $10 \times 10 \times 0.5$ mm^3 single-crystal magnesium oxide MgO(001) substrates were cleaned in sequential ultrasonic baths of trichloroethylene, acetone, and isopropyl alcohol for 20 min each, rinsed in de-ionized water, blown dry with nitrogen, mounted onto a Mo substrate holder using silver paint, and inserted into the deposition system which had a base pressure of 10^{-9} Torr. Prior to deposition, substrates were degassed for 1 hour at 1000 °C using a radiative pyrolytic graphite heater. Subsequently, the heater current was adjusted to reach the desired substrate temperature of 700 °C, as measured by a thermocouple underneath the substrate holder. 99.999% pure N_2, which was further purified with a MicroTorr purifier, was introduced into the chamber with a needle valve to reach a constant pressure of 5 mTorr, as measured with a capacitance manometer. 5 cm-diameter Ti (99.99%), Al (99.999%), and Mg (99.98%) targets were positioned 9, 23, and 9 cm from the substrate surface with −45°, 0°, and +45° tilt angles, respectively. All three targets were sputter etched for 5 min prior to deposition, using 100 W on each magnetron with a shutter shielding the substrate. A $Ti_{0.5}Mg_{0.5}N$ deposition rate of 3.8 nm min^{-1} was achieved using a constant power of 100 and 80 W to the titanium and magnesium targets, respectively. The dc power to the Al target was adjusted between 0 and 650 W to obtain a series of $(Ti_{0.5}Mg_{0.5})_{1-x}Al_xN$ with varying x = 0–0.44. During deposition, the substrate was continuously rotated at 60 rpm to ensure composition and thickness uniformity. A constant deposition time of 20 min for all layers yielded film thicknesses d = 75–135 nm, as determined by X-ray reflectivity (XRR) and scanning electron microscopy (SEM). Cross-sectional micrographs were obtained in a FEI Versa 3D field emission SEM with a 20 keV primary electron beam, using specimens that were prepared by cleaving samples along the [010] direction of the MgO(001) substrate. The layer thickness was determined from the micrograph by quantifying the intensity profile perpendicular to the substrate surface.

X-ray photoelectron spectroscopy (XPS) spectra were acquired using Al Kα radiation (1486.6 eV) in a PHI 5000 Versaprobe™ system with a hemispherical analyzer and an 8-channel detector. The samples were analyzed after exposure to air but without any sputter cleaning, such that the XPS results are not affected by preferential sputtering which has been reported to lead to, for example, a 12% reduction in the measured N-to-Ti ratio during sputter cleaning of TiN with 3 keV Ar^+ ions.[34,35] High-resolution spectra around the Al 2p, Mg 1s, Ti 2p and N 1s peaks were collected using a 23.5 eV pass energy, a 0.2 eV step size, and a 1.2 eV electron flood gun in conjunction with a low-energy (7 eV) ion neutralizer to compensate for possible surface charging. The composition was determined from the relative peak intensities corresponding to the area under the curves after background subtraction using the Shirley correction, and employing the relative sensitivity factors from the PHI MultiPak software package.

X-ray diffraction (XRD) was done using a Panalytical X'Pert PRO MPD system with a Cu Kα source and a hybrid mirror with a two-bounce two-crystal Ge(220) monochromator, yielding a parallel incident beam with a wavelength $\lambda_{K\alpha1}$ = 1.5406 Å,

a divergence of 0.0068°, and a width of 0.3 mm. Sample alignment included height adjustment as well as correction of the ω and χ tilt angles by maximizing the substrate peak intensity. Symmetric ω–2θ scans were obtained using a 0.04 radian Soller slit in front of a PIXcel line detector operated in receiving mode with a 0.165 mm active length, corresponding to a 2θ opening of less than 0.04°. ω-rocking curves were obtained using constant 2θ angles corresponding to (Ti, Mg, Al)N 002 reflections and using the same parallel beam geometry as used for ω–2θ scans. Asymmetric reciprocal space maps (RSMs) around 113 reflections were obtained using a small angle (below 15°) between the sample surface and the diffracted beam to cause beam narrowing which increases the 2θ resolution and therefore facilitates fast high-resolution reciprocal space mapping by taking advantage of parallel acquisition with all 255 channels of a line detector operated in scanning mode. In addition, ω–2θ scans with a divergent beam Bragg–Brentano geometry were acquired over a large 2θ range from 15–85° in order to detect small inclusions of possible secondary phases or misoriented grains.

Optical ultraviolet-to-visible (UV-Vis) transmittance T and reflectance R spectra were collected in an Agilent Cary 60 spectrophotometer over the wavelength range 190–1100 nm in 1.5 nm-steps. The reflectance spectra were obtained using a 6° incident angle and were calibrated using an Al mirror reference that was cross-calibrated with the reflection from a double-side polished MgO(001) substrate and optical constants for MgO from Palik's handbook.[36] The refractive index of the substrate as a function of wavelength was determined from R and T spectra of uncoated substrates by accounting for multiple reflections between the two air/MgO interfaces. It agrees well with the reported MgO refractive index[36] with deviations <4% for the majority of the wavelength range. All optical analyses assume normal incident light for reflection instead of the experimental 6°, which causes a negligible (<1%) error in the presented data. The collected spectra are treated using a three-media model (air/film/substrate) which assumes the light passing from air to a thin film of constant thickness and parallel surfaces (top and bottom) and then to the substrate.[26,37] The absorption within the MgO substrates is accounted for but results in a negligible correction in comparison to non-absorbing media for the investigated wavelength range. The optical absorption coefficient α is obtained from the measured T and R using $\alpha = \ln([1 - R]/T)/d$,[38] where d is the layer thickness. This approximate expression accounts for reflection at the layer surface but neglects multiple reflections within the layer, which have a negligible effect for sufficiently absorbing media. The R spectra are analyzed using a Drude–Lorentz model $\varepsilon(\omega) = \varepsilon_\infty - {\omega_p}^2/(\omega^2 - i\gamma_D\omega) + f_o{\omega_o}^2/({\omega_o}^2 - \omega^2 + i\gamma_o\omega)$, where the onset of interband transitions is modeled with a Lorentz oscillator with strength f_o, frequency ω_o, and damping factor γ_o. This single oscillator does not accurately describe the many interband transitions in (Ti, Mg, Al)N and is therefore not used to quantify interband transitions. However, it is nevertheless useful as it extends the energy range for data fitting of the reflection spectra from the near infrared region which is dominated by free carrier effects up to, and slightly into, the interband transition range. Higher energy transitions are accounted for by ε_∞, which is the dielectric constant for energies well above ω_o. The free carrier contribution is described with a classical Drude term, where the free carrier damping γ_D corresponds to the inverse of the carrier relaxation time τ, and the plasma frequency ω_p is related to the free carrier density N_e according to $\omega_p = \sqrt{N_e e^2/(\varepsilon_o \varepsilon_r m^*)}$ in SI units.[16] Here, e is the electron charge, ε_r the dielectric constant of the medium at optical frequencies, and m^* the electron effective mass.

First-principles density functional theory computations were performed with the Vienna *Ab initio* Simulation Package (VASP)[39] using the projector augmented wave (PAW)[40,41] method. Structural relaxations were done using the Perdew–Burke–Ernzerhof (PBE) generalized gradient approximation (GGA),[42] pseudo-potentials Ti_sv, Mg_pv, Al and N from the VASP database,[41] a plane wave energy cut-off of 520 eV, regular k-point meshes with 6000 k-points per reciprocal atom (KPPRA), Gaussian smearing with a 0.1 eV width, and a convergence limit for the electronic minimization $<10^{-6}$ eV per atom. The lattice parameters were determined as a function of the compositional parameter x in $(Ti_{0.5}Mg_{0.5})_{1-x}Al_xN$ alloys in the cubic rocksalt structure by generating Special Quasirandom Structures (SQS) with x = 0, 0.25, 0.5, 0.75 and 1. The SQS represents the completely disordered (random solid solution) configuration that is generated from Monte Carlo simulations with the cluster expansion method.[43–45] Each SQS is a 64-atom supercell with 32 N atoms on the anion sites and a mixture of Ti, Mg, and Al atoms on the 32 cation sites. Structural optimization was done by allowing the cell volume, shape and atomic positions to relax until the stress was minimized and the force on any atom was below 0.01 eV Å^{-1} as described in earlier works.[46,47] This results in relaxed super cells that are not perfectly cubic. However, the angles between the three relaxed unit vectors deviate by less than 1° from normal and their lengths differ by less than 1%, such that the deviation from cubic is assumed to be negligible and a single lattice constant is determined from the calculated unit cell volume.

Bandgaps were determined using hybrid functional calculations according to Heyd–Scuseria–Ernzerhof (HSE06)[48] which use a 75%/25% mix of PBE and Hartree–Fock (HF) functionals. These calculations are done for the 64-atom SQS supercells with x = 0–0.75 as relaxed with PBE but without further relaxation, and using 2 × 2 × 2 k-point grids, a 450 eV energy cutoff, and pseudopotentials that include the 2s and 2p electrons for Mg and 3s and 3p electrons for Ti in the cores. The fundamental bandgaps were determined from the difference between the conduction band minimum and the valence band maximum, where the former is obtained from the plotted density of states (DOS) using data fitting that assumes the conduction band DOS $\propto E^{1/2}$. The (HSE06) electronic structure of rocksalt AlN (x = 1) was calculated using a two-atom primitive unit cell and the same computational parameters as for the 64-atom supercells but a 10 × 10 × 10 k-point grid. This provides values for both the fundamental indirect gap as well as the lowest-energy direct interband transition (direct gap). A relaxed 4-atom tetragonal unit cell which corresponds to an ordered $Ti_{0.5}Mg_{0.5}N$ (x = 0) with Ti and Mg atoms on alternating (001) planes was

used to estimate the direct transition from the gap between filled and empty states for the *k*-point that corresponds to the X point of the Brillouin zone of a 2-atom rocksalt structure primitive unit cell.

Results and discussion

Fig. 1 summarizes the results from the compositional analyses by photoelectron spectroscopy, showing a plot of the Al content in the layers as a function of power P_{Al} applied to the Al target during deposition. The measured N-to-metal ratio is approximately unity for all layers, ranging from 0.98–1.06 as listed in the inset in Fig. 1. Thus, within experimental uncertainty, the layers exhibit a stoichiometric 1 : 1 cation-to-anion ratio, as expected for a rocksalt structure solid solution. The Mg content is listed in the table as the fraction of the sum (Ti + Mg). It is 0.46 ± 0.01 for all layers, indicating that the compounds contain approximately equal fractions of Ti and Mg, as intended. Correspondingly, we use the notation $(Ti_{0.5}Mg_{0.5})_{1-x}Al_xN$ to represent all samples in this paper. The table also includes the layer thickness d which is measured by XRR for $d < 120$ nm and by SEM for $d > 120$ nm. A typical cross-sectional SEM micrograph from the P_{Al} = 650 W layer is shown as inset, indicating a relatively flat top surface and smooth substrate-layer interface, and a relatively sharp contrast between substrate, layer, and vacuum which is used to determine d = 135 ± 10 nm with a contrast profile analysis. d increases from 75 to 135 nm as P_{Al} increases from 0 to 650 W, while both the deposition time and the power to the Ti and Mg targets during deposition are kept fixed. Thus, this increase in d is attributed to an increasing Al content in the deposited $(Ti_{0.5}Mg_{0.5})_{1-x}Al_xN$ layers and can be used to directly quantify x. The resulting values are plotted as blue circles in Fig. 1, and are in excellent agreement with the red squares from XPS measurements. More specifically, the plot shows that x increases approximately linearly from zero for $(Ti_{0.5}Mg_{0.5})N$ to x = 0.09 (0.052), 0.22 (0.222), 0.33 (0.331), and 0.44 (0.443) for P_{Al} = 140, 300, 435, and 650 W, where the values in parenthesis are those obtained from the thickness analysis, indicating deviations of $\Delta x < 0.04$ for the two independent measurements. We note that the uncertainty in the values in parenthesis is ±0.02–0.04 but that they are nevertheless given with three significant figures to indicate the level of agreement with the x-values from the XPS analyses.

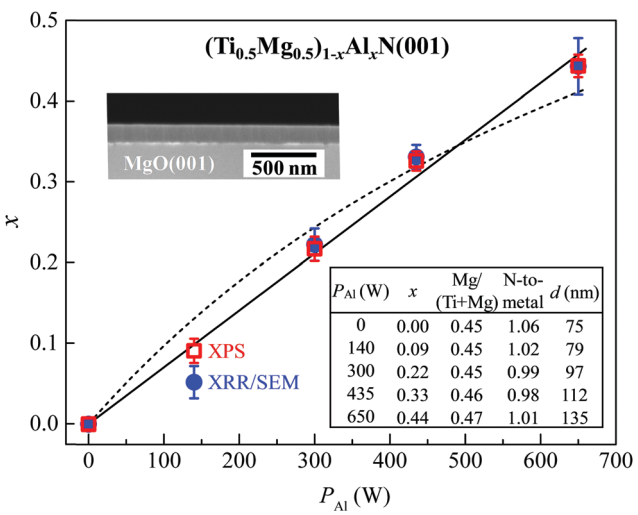

Fig. 1 The Al content x in $(Ti_{0.5}Mg_{0.5})_{1-x}Al_xN$ layers *vs.* the power P_{Al} applied to the Al target during deposition, as determined from XPS measurements and thickness analyses done by XRR and SEM. The solid and dashed lines are from curve fitting, assuming that x or the Al deposition rate is proportional to P_{Al}, respectively. The insets show a cross-sectional SEM micrograph used to determine the thickness d = 135 nm for the P_{Al} = 650 W layer, and a table that lists the measured composition and d for each sample. The Mg and N content are given relative to the sum Mg + Ti and the total metal content Mg + Ti + Al, respectively.

The solid line through the data points is the result from linear curve fitting, indicating that the Al content x in $(Ti_{0.5}Mg_{0.5})_{1-x}Al_xN$ increases linearly with P_{Al}. We note, however, that such a linear increase is only expected for small x values, while assuming an Al deposition rate that is proportional to P_{Al} would yield an expected composition $x = P_{Al}/(P_{Al} + C)$. Here C corresponds to P_{Al} that results in x = 0.5. It is determined to be C = 930 W from curve fitting, which also yields the dashed line in Fig. 1. The dashed line clearly overestimates the Al content for small P_{Al}. We attribute this to poisoning of the Al target surface by the formation of insulating AlN patches that reduce the sputtering yield particularly at low sputtering rates for which removal of AlN from the target surface is limited. Conversely, the energetic flux between the cathode and the substrate at high P_{Al} facilitates directional transport of sputtered atoms, minimizing scattering and thermalization of Al atoms in the vapor phase and results in the measured x above the dashed line for P_{Al} = 650 W. This latter effect has previously been referred to as sputter wind.[49,50]

Fig. 2 shows sections of typical X-ray diffraction ω–2θ patterns for 2θ = 41.7–43.1° from $(Ti_{0.5}Mg_{0.5})_{1-x}Al_xN$ layers with x = 0.00–0.44, as labeled. The intensity is plotted on a logarithmic scale and the scans are offset vertically for clarity purposes. All patterns exhibit a MgO 002 substrate peak at 2θ = 42.89°, corresponding to a lattice constant a_o = 4.214 ± 0.002 Å which is in agreement with the published 4.212 Å from bulk MgO crystals.[51] In addition, they show a peak in the range 2θ = 42.1°–42.7° which is attributed to the $(Ti_{0.5}Mg_{0.5})_{1-x}Al_xN$ 002 reflection. These are the only detectable peaks over the entire measured 2θ = 15°–85° range, indicating strong preferred 001 orientation of the $(Ti_{0.5}Mg_{0.5})_{1-x}Al_xN$ layers for all samples. The pattern from the $Ti_{0.5}Mg_{0.5}N$ layer (x = 0.00) has a peak at 42.16°, corresponding to an out-of-plane lattice constant $a_\perp$ = 4.283 Å. This is within the range of previously reported values of 4.279–4.295 Å for $Ti_{0.5}Mg_{0.5}N$/MgO(001) layers deposited by magnetron sputtering.[26,27,31,52] We attribute the variation in reported lattice constants to different levels of strain relaxation, which depends on the growth temperature and layer thickness[31] and is quantified and discussed for the samples in this study further below. The alloy film with x = 0.09 yields a similar XRD pattern as for $Ti_{0.5}Mg_{0.5}N$, however, with the layer peak shifted to the right to 2θ = 42.26°, corresponding to a lattice parameter in the growth direction $a_\perp$ = 4.273 Å. Increasing the Al concentration further

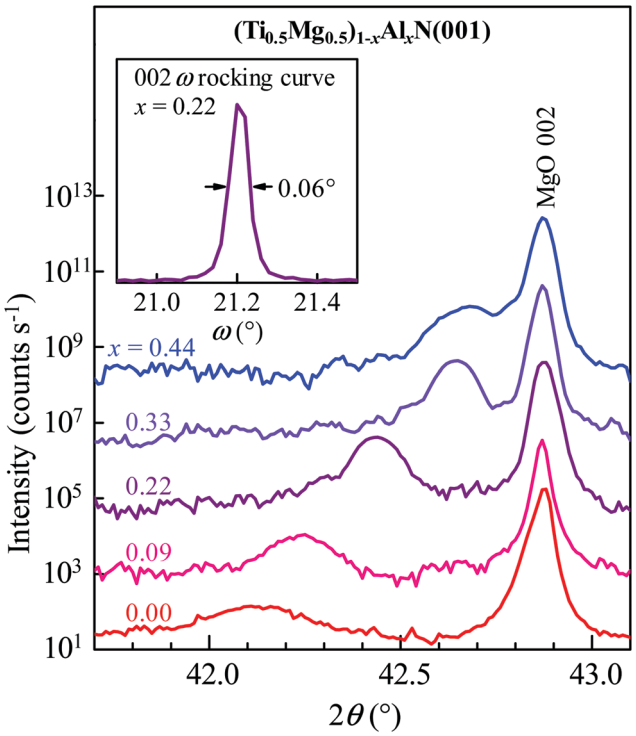

Fig. 2 X-ray diffraction ω–2θ scans from $(Ti_{0.5}Mg_{0.5})_{1-x}Al_xN(001)$ layers on MgO(001) with x = 0–0.44. The inset shows a typical ω rocking curve from the 002 reflection of the x = 0.22 layer.

to x = 0.22, 0.33, and 0.44 leads to a continuous peak shift to larger 2θ-values of 42.47°, 42.68°, and 42.71°, yielding a decreasing $a_\perp$ = 4.254, 4.234, and 4.231 Å, respectively. This decrease is expected based on the lattice constant of rocksalt structure AlN of 4.045 Å[53] which is 5% smaller than that for $Ti_{0.5}Mg_{0.5}N$. In addition, the layers with a large Al content also have a narrower and more intense $(Ti_{0.5}Mg_{0.5})_{1-x}Al_xN$ 002 peak. More specifically, the peak intensity from layers with x = 0.09, 0.22, and 0.33 is 1.1, 4.3 and 17 times stronger than that for $Ti_{0.5}Mg_{0.5}N$, and the peak full-width at half-maximum (FWHM) decreases from $\Gamma_{2\theta}$ = 0.23° for x = 0.00 to $\Gamma_{2\theta}$ = 0.13°, 0.10° and 0.09° for x = 0.09, 0.22, and 0.33, respectively, indicating an increasing crystalline quality which is primarily attributed to a decreasing lattice mismatch. The out-of-plane coherence length, which corresponds to average mosaic domain size for coherent X-ray scattering along the film growth direction, is 94 and 111 nm for x = 0.22 and 0.33, respectively, as determined using $\xi_\perp = \lambda/(\Gamma_{2\theta}\cos\theta)$.[31] These values match the measured layer thicknesses d = 97 and 112 nm, indicating that $\xi_\perp$ is limited by d and that peak broadening from possible crystalline defects and strain variations along the growth direction are below the detection limit.[54] This trend is not continued to x = 0.44, which results in a peak intensity that is only 3.4 times stronger than that for $Ti_{0.5}Mg_{0.5}N$ and a $\Gamma_{2\theta}$ = 0.10° yielding $\xi_\perp$ = 94 nm. The latter value is 31% below d = 135 nm and indicates the onset of crystalline deterioration for x = 0.44. This is attributed to a decreasing phase stability with increasing x. Layers with an even higher Al content deposited using P_{Al} = 750 and 850 W (not shown) exhibit only weak $(Ti_{0.5}Mg_{0.5})_{1-x}Al_xN$ 002 reflections and an extra peak at $2\theta \approx 43.40°$, suggesting the formation of a $Ti_{1-x}Al_xN$ or related phase[55] and a reduced crystalline quality.

The inset in Fig. 2 shows a typical XRD ω rocking curve of the 002 reflection from the $(Ti_{0.5}Mg_{0.5})_{0.78}Al_{0.22}N$ layer, which is obtained using a constant 2θ = 42.47° and plotted in a linear scale. Its FWHM Γ_ω = 0.06° is quite small in comparison to other epitaxial rocksalt structure nitrides with reported values ranging from 0.14–2.20°[20,21,25,56–61] and indicates a strong crystalline alignment of the $(Ti_{0.5}Mg_{0.5})_{0.78}Al_{0.22}N$ 001 planes. The rocking curve width is relatively small for all layers, with Γ_ω = 0.42°, 0.29°, 0.04°, and 0.05° for x = 0.00, 0.09, 0.33, and 0.44, respectively. The smallest Γ_ω value in this list is from the $(Ti_{0.5}Mg_{0.5})_{0.67}Al_{0.33}N$ layer which also exhibits the largest peak intensity in the main plot. Thus, the observed increasing peak intensity and decreasing $\Gamma_{2\theta}$ and Γ_ω are consistent and show the increasing crystalline quality with increasing $x < 0.44$.

Fig. 3 shows high-resolution XRD reciprocal space maps (RSMs) acquired about asymmetric 113 reflections from five $(Ti_{0.5}Mg_{0.5})_{1-x}Al_xN(001)$/MgO(001) layers. They are shown as color filled iso-intensity contour maps plotted in a logarithmic scale within k-space where $k_\perp = 2\sin\theta\cos(\omega-\theta)/\lambda$ and $k_\parallel = 2\sin\theta\sin(\omega-\theta)/\lambda$ correspond to directions perpendicular and parallel to the substrate surface along perpendicular [001] and [110] directions, respectively, as indicated by the labeled arrows. The figure also includes a scale bar in units of reciprocal length ($Å^{-1}$) and arrows indicating the experimental ω–2θ and ω scan directions. The five strong peaks on the top of each panel are due to MgO 113 substrate reflections, while the lower peaks are from $(Ti_{0.5}Mg_{0.5})_{1-x}Al_xN$ 113. The dashed lines that connect the center of the MgO and layer 113 reflections serve as an indicator to gauge the degree of strain relaxation, as discussed below. We note that the broadening of the MgO 113 peak along the ω-direction is associated with small-angle grain boundaries in the single crystal substrates while the elongation from the top-left toward the bottom-right are intrinsic resolution streaks associated with the Ge(220) crystal in the hybrid monochromator.[62]

The out-of-plane $a_\perp$ and in-plane $a_\parallel$ lattice constants are determined from the peak positions. For example, the 113 peaks

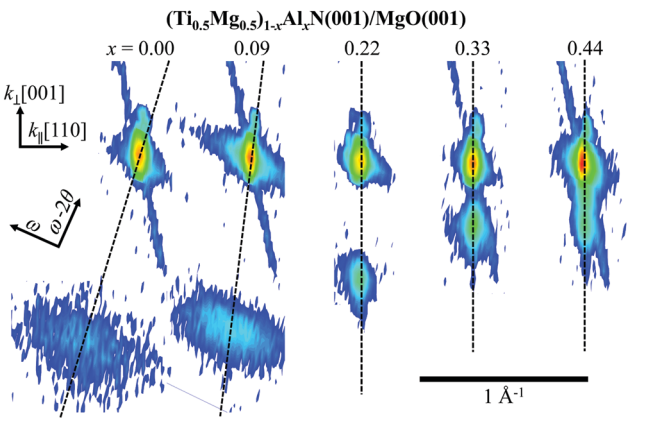

Fig. 3 RSMs about asymmetric 113 reflections from five $(Ti_{0.5}Mg_{0.5})_{1-x}Al_xN(001)$/MgO(001) layers.

from the $Ti_{0.5}Mg_{0.5}N$ (x = 0.00) sample are at $k_\perp$ = 7.122 nm^{-1} and $k_\parallel$ = 3.357 nm^{-1} for the MgO substrate and $k_\perp$ = 7.011 nm^{-1} and $k_\parallel$ = 3.323 nm^{-1} for the layer, yielding $a_\perp = a_\parallel = 4.212 \pm 0.001$ Å for MgO and $a_\perp = 3/k_\perp = 4.279 \pm 0.001$ Å and $a_\parallel = \sqrt{2}/k_\parallel = 4.255 \pm 0.002$ Å for $Ti_{0.5}Mg_{0.5}N$. These values are in agreement with the out-of-plane lattice parameters of 4.214 ± 0.002 Å for MgO and 4.283 ± 0.002 Å for $Ti_{0.5}Mg_{0.5}N$ determined from the ω–2θ scans shown in Fig. 2. The $Ti_{0.5}Mg_{0.5}N$ out-of-plane lattice parameter is larger than the in-plane lattice parameter, suggesting a mild in-plane compressive strain $\varepsilon_\parallel = (a_\parallel/a_o - 1) = -0.35\%$, where the relaxed lattice constant a_o is determined using $a_o = (a_\perp - \nu a_\perp + 2\nu a_\parallel)/(1+\nu) = 4.270$ Å and ν is the Poisson's ratio which is assumed to be a composition-independent constant of 0.22.[63,64] This assumption has a negligible effect on the uncertainty in a_o, since a change in ν from 0.22 to, for example, 0.25 causes a correction in a_o of only 0.02%. Our a_o = 4.270 Å is in good agreement with previous studies that have determined the relaxed lattice constants and reported values ranging from 4.265–4.273 Å.[26,27,31] The −0.35% compressive strain is attributed to a −1.4% misfit between the lattice constants of $Ti_{0.5}Mg_{0.5}N$ and MgO. The strain is smaller than the misfit, indicating that the layer is partially relaxed. More specifically, the degree of relaxation $\delta = (a_\parallel - a_{MgO})/(a_o - a_{MgO}) = 74\%$ for the x = 0.00 layer. The relaxation of this layer is also evident from the tilt in the dashed line in the plotted map which indicates a left-shift of the layer peak in comparison to the substrate peak, and therefore $a_\parallel > a_{MgO}$. The map from the x = 0.09 layer also exhibits a layer peak that is located below and to the left of the MgO 113 reflection, indicating partial relaxation with δ = 38%. The x = 0.09 peak is shifted upwards in comparison to the x = 0.00 peak, indicating a smaller out-of-plane lattice constant $a_\perp$ which is attributed to a decreasing a_o with increasing x, as discussed below. The elliptical shape of the 113 reflections from these two layers (x = 0.00 and 0.09) in reciprocal space can be described by peak broadening along the two primary ω–2θ and ω scan directions, which are rotated by 25.24° from the $k_\perp$ and $k_\parallel$ directions. The broadening along ω–2θ is attributed to local strain variations and the finite layer thickness, while broadening along ω is primarily due to the mosaic spread, that is, the misalignment of crystallites which are single crystal blocks within the epitaxial $(Ti_{0.5}Mg_{0.5})_{1-x}Al_xN$ layer. We note that the 113 reflection from x = 0.09 is more confined in both ω–2θ and ω direction and also 2 times more intense than that of $Ti_{0.5}Mg_{0.5}N$, indicating a reduced crystalline mosaicity and improved crystalline quality, consistent with ω–2θ scans and ω-rocking curves discussed above.

The three RSMs on the right in Fig. 3 are from $(Ti_{0.5}Mg_{0.5})_{1-x}Al_xN$ layers with x = 0.22, 0.33 and 0.44. Their $(Ti_{0.5}Mg_{0.5})_{1-x}Al_xN$ 113 peaks are vertically aligned with the MgO 113 substrate peaks, indicating that these layers are fully strained (δ = 0) with $a_\parallel = a_{MgO}$. The layer peaks shift upwards with increasing x, continuing the trend from x = 0.00 and 0.09 which is due to a decreasing lattice constant. This also results in a decreasing in-plane biaxial compressive strain from −0.63% for x = 0.22 to $\varepsilon_\parallel$ = −0.35% and −0.34% for x = 0.33 and 0.44, respectively. The $(Ti_{0.5}Mg_{0.5})_{1-x}Al_xN$ 113 peaks are vertically elongated, which is primarily attributed to the finite layer thickness, consistent with the above discussion on the 002 peak widths. The RSMs shown in Fig. 3 confirm, in combination with the results from Fig. 2, that all $(Ti_{0.5}Mg_{0.5})_{1-x}Al_xN$ layers in this study are epitaxial single crystals and that they exhibit a cube-on-cube epitaxial relationship with the substrate: $(001)_{TiMgAlN}\|(001)_{MgO}$ and $[100]_{TiMgAlN}\|[100]_{MgO}$.

Fig. 4 is a plot of the out-of-plane $a_\perp$, in-plane $a_\parallel$, and relaxed a_o lattice constants *vs.* x in $(Ti_{0.5}Mg_{0.5})_{1-x}Al_xN$, as determined by XRD analyses, and the lattice constants determined from our first-principles calculations. The plot includes two datasets for $a_\perp$ indicated by open and solid red triangles, as obtained from the 002 peak position in ω–2θ scans and from the $k_\perp$ values of the 113 reflection measured using RSMs, respectively. There is good overall agreement between these two distinct measurements from the same sample set with deviations of only 0.01–0.11%. The $a_\perp$ values decrease with increasing x, indicating a decreasing lattice constant with increasing Al content, as mentioned above and discussed below. Similarly, the plotted $a_\parallel$ decreases initially with x but becomes independent of x for $x \geq 0.22$. More specifically, the measured $a_\parallel$ for x = 0.22, 0.33, and 0.44 ranges from 4.211–4.213 Å which is, within experimental uncertainty, identical (±0.03% deviation) to the lattice constant of the substrate a_{MgO} = 4.212 Å. This is also illustrated by the black horizontal solid line in Fig. 4 and is consistent with these layers being fully strained. The blue squares in Fig. 4 represent the relaxed lattice constant a_o which decreases from 4.270 Å for $Ti_{0.5}Mg_{0.5}N$ (x = 0) to a_o = 4.255, 4.239, 4.226 and 4.226 Å for the layers with x = 0.09, 0.22, 0.33 and 0.44, respectively. The solid blue line indicates that the data points

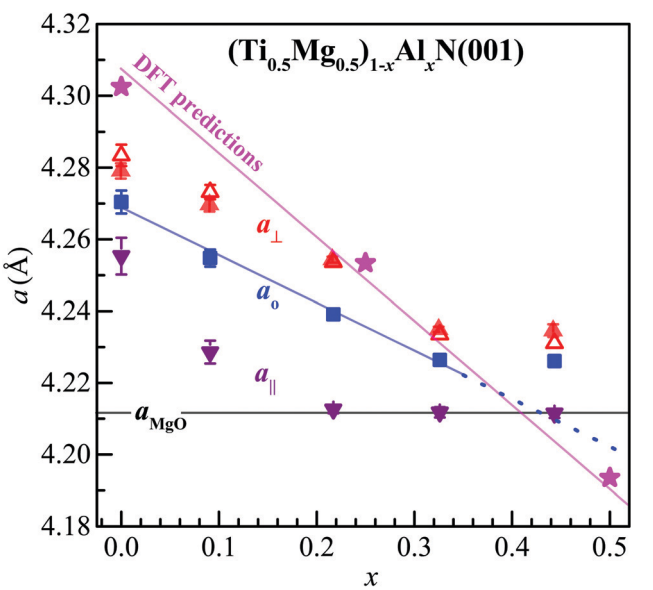

Fig. 4 Out-of-plane $a_\perp$, in-plane $a_\parallel$, and relaxed a_o lattice constants obtained from RSMs (red up-triangles, purple down-triangles, and blue squares) and $a_\perp$ obtained from symmetric ω–2θ scans (red open triangles) *vs.* Al content x in $(Ti_{0.5}Mg_{0.5})_{1-x}Al_xN(001)/MgO(001)$ layers. The lattice constants from first-principles calculations and the associated linear fit are plotted as magenta stars and solid line.

for $x \leq 0.33$ are well described by a linear relationship: $a_o = (4.269 - 0.131x)$ Å. Extrapolating this linear relationship to $x = 1$ predicts a lattice constant for rocksalt structure AlN of 4.138 Å. This is 2% larger than the previously reported 4.04–4.08 Å from experiments on rocksalt structure AlN[65,66] and suggests a positive bowing for the $(Ti_{0.5}Mg_{0.5})_{1-x}Al_xN$ system if the rocksalt phase could be synthesized over the entire composition range $0 \leq x \leq 1$. We note that the measured $a_o = 4.226$ Å for the $x = 0.44$ layer is above the linear trend indicated by the blue line. This is opposite to the expectation based on positive bowing and is attributed to a possible Al-deficiency in the rocksalt $(Ti_{0.5}Mg_{0.5})_{1-x}Al_xN$ phase. More specifically, a_o of this layer matches the lattice constant measured for $x = 0.33$, suggesting that only 33% of the cations in the rocksalt phase are Al, while the remainder of the Al is incorporated in secondary phases with a nanocrystalline structure that cannot be detected by our XRD measurements. Some evidence for this hypothesis is the deteriorated crystalline quality for $x = 0.44$ and the observation of distinct secondary-phase XRD peaks from samples with $P_{Al} \geq 750$ W, as discussed above.

Fig. 4 also includes the results from first-principles density functional theory calculations using 64-atom special quasi-random structures of $(Ti_{0.5}Mg_{0.5})_{1-x}Al_xN$ alloys with $x = 0$–1. The predicted lattice constant for $Ti_{0.5}Mg_{0.5}N$ ($x = 0$) is 4.302 Å, which is within the range 4.266–4.315 Å of previously reported first principles calculations for $Ti_{0.5}Mg_{0.5}N$.[19,67] The lattice constant decreases with increasing Al content to 4.253 and 4.194 Å for $Ti_{0.375}Mg_{0.375}Al_{0.25}N$ and $Ti_{0.25}Mg_{0.25}Al_{0.5}N$, as indicated by the star-shaped data points in Fig. 4 at $x = 0.25$ and 0.5, respectively. Increasing the Al content further (not shown) yields $a = 4.133$ Å for $x = 0.75$ and $a = 4.070$ Å for rocksalt AlN ($x = 1$). The latter value is in good agreement with the previously reported 4.016–4.067 Å from first-principles predictions[68,69] and 4.04–4.08 Å from experiments on rocksalt structure AlN.[65,66] The solid magenta line in Fig. 4 corresponds to $a = (4.308 - 0.234x)$ Å and is a linear fit to the first-principles results for $x = 0$–1. It indicates that the predicted lattice constant is 0.1–0.7% above the experimental a_o for $0 \leq x \leq 0.33$. This overestimation is primarily attributed to the common overestimation of lattice constants by the GGA.[70] We note that the slope da/dx from the calculations is 80% steeper than from experiment and that the predicted da/dx is composition independent over the entire range $x = 0$–1. Thus, our first-principles simulations do not provide any evidence for the positive bowing that is suggested by our measured lattice constants. This disagreement may suggest that only a fraction of the Al incorporates into the rocksalt solid solution, similar to the above explanation for the lattice constant deviation at $x = 0.44$. With this explanation, the extra Al would form nanoclusters in the nitride matrix that cannot be directly detected by XRD. However, we expect that the strain fields and the crystal discontinuity caused by such clusters would reduce the measured crystalline quality, contrary to our experimental results. In addition, the good agreement between composition determination from XPS and thickness measurements in Fig. 1 provide no evidence for Al surface segregation. We also note that Al-rich rocksalt structure nitrides including $Ti_{1-x}Al_xN$ are known to exhibit spinodal decomposition which may lead to nearly amorphous Al-rich inclusions that are not detected by XRD[71] but, similarly to metallic Al clusters, are expected to lead to local strain fields and a decay in the crystalline quality which is not detected for $x \leq 0.33$.

Fig. 5 is a plot of the optical carrier density N^* as a function of the Al content x in $(Ti_{0.5}Mg_{0.5})_{1-x}Al_xN(001)$ layers. We define N^* as the true carrier density N_e scaled by the inverse of the dielectric constant due to core polarization ε_r times the ratio m^*/m_e of the optical electron effective mass divided by the electron mass, thus $N^* = N_e \cdot m_e/(\varepsilon_r m^*)$. Correspondingly, N^* can be directly determined from the plasma frequency using $N^* = \omega_p^2 \varepsilon_o m_e / e^2$. A typical reflection R spectrum from an $x = 0.22$ layer is shown in the inset of Fig. 5 for the photon energy range $\hbar\omega = 1.1$–3.0 eV. It includes the result from curve fitting (red line) using a Drude–Lorentz model to determine ω_p and subsequently N^*. The fitted curve matches well the measured data, indicating the $(Ti_{0.5}Mg_{0.5})_{0.78}Al_{0.22}N$ optical properties are well described by the Drude–Lorentz model for the presented frequency range. Similar data fitting is done for the reflection spectra from all layers, yielding the N^* *vs.* x data that is plotted in the main part of Fig. 5. $N^* = 1.39 \times 10^{22}$ cm^{-3} for $Ti_{0.5}Mg_{0.5}N$ ($x = 0.00$), which is relatively large and can be attributed to the free electrons from excessive Ti atoms. More specifically, the measured Ti-to-Mg ratio for this layer is 0.55 : 0.45, as indicated in Fig. 1, suggesting that 10% of the cation sites are occupied by excess Ti atoms which may each provide one electron to the conduction band, resulting in a heavily degenerate semiconductor

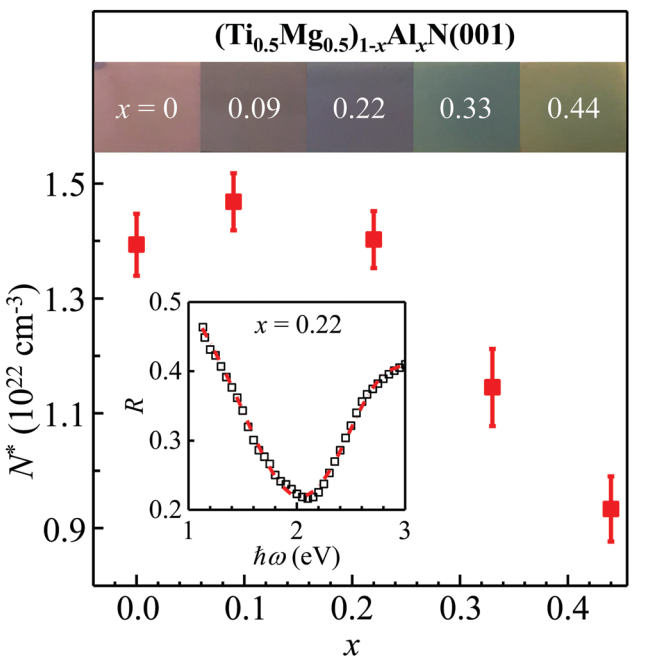

Fig. 5 Optical carrier density N^* as a function of Al content x in $(Ti_{0.5}Mg_{0.5})_{1-x}Al_xN(001)$ layers. The inset shows a typical measured reflection R spectrum for $x = 0.22$ (open squares), fitted with the Drude–Lorentz model (dashed line) for photon energies $\hbar\omega = 1.1$–3.0 eV. The top inset indicates the apparent color observed for the samples as detected with an optical camera.

with an expected $N_e = 5.1 \times 10^{21}$ cm^{-3}. This value is 2.7 times smaller than N^* from the optical analysis, suggesting an effective mass $m^* = m_e/(2.7\varepsilon_r)$ which is smaller than a previously reported prediction for the density-of-states effective mass for $MgTiN_2$ of $m^* = 1.4m_e$.[24] We note that the related rocksalt nitride semiconductor ScN has also been reported to be heavily n-type degenerate, which is attributed to O, F, or Ta impurities,[9,20,21,72] and that even $Sc_{1-x}Mg_xN$ compounds with $x \leq 0.025$ exhibit n-type carriers.[9] Oxidation has been reported to be important for the related $Mg_xZr_{2-x}N_2$ compound for Mg-rich compositions,[25,73] and causes the development of an n-type doped oxynitride with metallic conduction on the surface of CrN and $Cr_{1-x}Al_xN$ without, however, affecting the bulk of the layers.[33,74] Similarly, we do not expect that oxidation affects electron transport in our $(Ti_{0.5}Mg_{0.5})_{1-x}Al_xN(001)$ layers, since $Ti_{1-x}Mg_xN$ has been reported to exhibit a high oxidation resistance.[52,75,76]

The main plot in Fig. 5 shows that the addition of Al causes an initial slight increase to $N^* = 1.47 \times 10^{22}$ cm^{-3} for $x = 0.09$, followed by a decrease to 1.40, 1.15, and 0.93×10^{22} cm^{-3} for $x = 0.22$, 0.33, and 0.44, respectively. This is also summarized in Table 1, which additionally includes the measured resistivity ρ of the same samples at both room temperature (295 K) and 77 K. We attribute the initial increase in N^* and the related decrease in ρ to a reduction in the dislocation density which is due to the decrease in the strain relaxation from 74 to 38% that also causes an increase in the crystalline quality quantified by the XRD results shown in Fig. 2 and 3. Dislocations may (i) cause trap states that reduce N_e,[12,13,21] (ii) act as scattering centers for conduction electrons which increases the resistivity,[77,78] and (iii) result in increased weak localization that leads to a higher ρ and a more negative temperature coefficient of resistivity TCR. Consistent with these arguments, the increase from $x = 0$ to 0.09 results in a 2.5-fold decrease in the room-temperature resistivity and an increase in the average TCR between 77 and 295 K from -1.04 μΩ cm K^{-1} to a small -0.03 μΩ cm K^{-1}. A further increase in the Al content to $x = 0.22$–0.44 results in a continuous decrease in N^* and a corresponding increase in ρ as well as a decrease in TCR to more negative values. This suggests an increasing carrier localization which may be attributed to (i) the increasing bandgap that causes the states from excess Ti to be further below the conduction band edge and (ii) an increasing randomization of cation site occupation that leads to weak Anderson localization that has been reported for epitaxial layers of other transition metal nitrides including CrN(001),[77,79] WN(001),[80] TaN_x(001),[60,81] HfN_x(001),[82] NbN(001),[56] $Sc_{1-x}Ti_xN$(001)[38] and $Ti_{1-x}W_xN$(001).[83] We note that the relative increase in ρ with increasing Al content is more pronounced than the relative decrease in N^*. This is primarily attributed to a decreasing mobility with increasing x, caused by the random arrangement of Ti, Mg and Al atoms on cation sites that effectively reduce the localization length.

Table 1 The optical career density N^*, and the resistivity measured at both 77 and 295 K, for $(Ti_{0.5}Mg_{0.5})_{1-x}Al_xN(001)$ layers as a function of x

		ρ (10^{-6} Ω m)	
x	N^* (10^{22} cm^{-3})	77 K	295 K
0.00	1.39	9.0	6.8
0.09	1.47	2.8	2.7
0.22	1.40	8.9	6.7
0.33	1.15	40	21
0.44	0.93	708	89

The top inset in Fig. 5 is a photograph of the $(Ti_{0.5}Mg_{0.5})_{1-x}Al_xN$/MgO(001) samples, sorted according to their composition x. They exhibit distinct colors, transitioning from light to dark magenta for $x = 0$ and 0.09, and then to indigo, green, and yellow for $x = 0.22$, 0.33, and 0.44, respectively. The colors are consistent with the measured optical reflection spectra, provided as ESI† (Fig. S1). More specifically, the magenta color for $x = 0.00$ and 0.09 is attributed to local reflection maxima at 1.7, 2 and 3 eV that lead to a mixture of violet, orange and red. The lighter magenta for $x = 0.00$ is due to its higher reflection at 2 eV while a dominant reflection above 3 eV gives the $x = 0.09$ sample a darker color. Increasing the Al content leads to a red shift of the reflection edge, such that the color is purely attributed to interband transitions which result in reflection maxima at 450, 550, and 600 nm, yielding indigo, green, and yellowish colors for $x = 0.22$, 0.33, and 0.44, respectively. We note that the yellow color here is distinctly different from the well-known golden yellow color for pure TiN, which is a mixture of reflected yellow, orange and red due to free carriers and a reflection edge at around 2 eV.[14]

Fig. 6 is a plot of the optical absorption coefficient α *vs.* photon energy $\hbar\omega = 1.1$–4.0 eV for $(Ti_{0.5}Mg_{0.5})_{1-x}Al_xN$/MgO(001) layers with $x = 0$–0.44. The minor discontinuities around $\hbar\omega = 1.75$ eV are experimental artifacts due to the switch of the optical gratings and the associated beam shift. The absorption at low photon energies ($\hbar\omega < 2$ eV) is caused by free carriers,

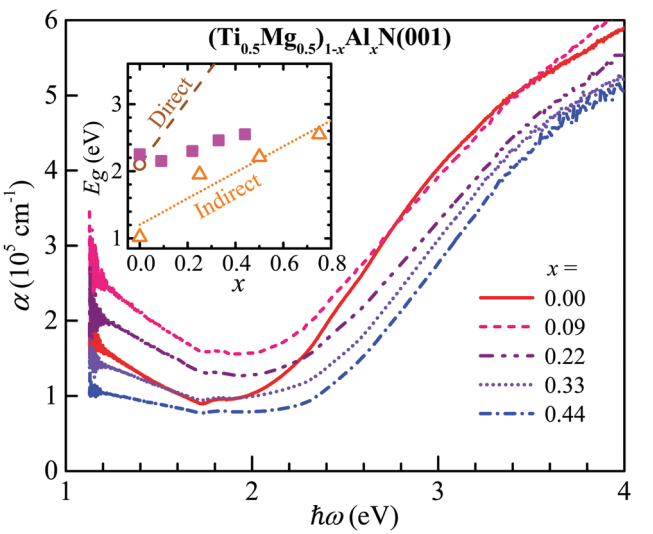

Fig. 6 Optical absorption coefficient α *vs.* photon energy $\hbar\omega = 1.1 - 4.0$ eV for $(Ti_{0.5}Mg_{0.5})_{1-x}Al_xN$/MgO(001) layers, as determined from transmission and reflection spectra. The inset shows the measured optical bandgap E_g (magenta squares), the fundamental indirect gap calculated using SQS supercells and a hybrid functional (orange open triangles), the calculated direct transition energy at $x = 0$ (open circle), and dashed and dotted lines from a linear fit to the calculated direct and indirect gaps, respectively.

while the increase above 2 eV is due to interband transitions. More specifically, the low-energy absorption at, for example, $\hbar\omega$ = 1.2 eV is 1.6 × 10^5 cm^{-1} for $Ti_{0.5}Mg_{0.5}N$ (x = 0), increases to 2.5 × 10^5 cm^{-1} for x = 0.09, and then decreases to 2.0, 1.4, 1.0 × 10^5 cm^{-1} for x = 0.22, 0.33, and 0.44, respectively. This trend replicates the measured carrier concentration and is consistent with the above arguments on $N^*(x)$. The absorption onset due to valence-to-conduction interband transitions is quantitatively analyzed using the Tauc plot method.[20] A linear extrapolation of $(\alpha\hbar\omega)^2$ *vs.* $\hbar\omega$ curves to $(\alpha\hbar\omega)^2$ = 0 yields values for the optical gaps E_g = 2.3, 2.2, 2.3, 2.5, and 2.6 eV for x = 0, 0.09, 0.22, 0.33, and 0.44, as plotted in the inset of Fig. 6. The inset also includes the calculated fundamental (indirect) gap E_g^I values, as determined from SQS supercells and denoted by orange open triangles. E_g^I = 1.0, 2.0, 2.2 and 2.6 eV for x = 0.00, 0.25, 0.50, and 0.75. The x = 0 value of 1.0 eV is slightly smaller than the previously predicted 1.33 eV for disordered $Ti_{0.5}Mg_{0.5}N$ using the HSE06 functional.[19] The rocksalt structure AlN (x = 1) has a calculated (indirect) gap of 5.8 eV and a lowest-energy direct transition of 6.9 eV. These values are well above the increasing trend indicated by the triangles and the dotted line, and are outside of the plotted range. They are comparable to the bandgap of 5.90–6.25 eV for wurtzite AlN,[72,84–88] but are larger than 4.7 and 4.9 eV determined from extrapolating optical measurements on $Al_{1-x}Sc_xN$(001) layers.[21,89] They are also larger than the previously reported 4.5–5.0 eV for rocksalt structure AlN obtained with the conventional GGA,[69,90] consistent with the well-known underestimation of bandgaps using standard density functionals. The inset also shows the calculated direct transition of 2.1 eV at x = 0 (as open brown circle), as determined from an ordered $Ti_{0.5}Mg_{0.5}N$ alloy described in the Methods Section, as well as a dashed line that connects this value with 6.9 eV for x = 1, indicating the expected direct transition energy *vs.* x under the assumption of a perfectly linear bandgap *vs.* composition dependence.

Our measured $E_g(Ti_{0.5}Mg_{0.5}N)$ = 2.3 eV at x = 0 is very close to our predicted 2.1 eV direct transition energy, is just slightly above the 2.0 eV reported for magnetron sputtered $TiMgN_2$ layers,[24] and is in excellent agreement with 2.3 eV from other optical studies[26,27] which attribute the absorption onset to N-2p to Ti-3d(t_{2g}) transitions. Our measured optical gap E_g increases with increasing Al content, but only by 0.3 eV for x = 0 to 0.44. This increase is much weaker than the slope of the dashed line, suggesting that the direct gap may exhibit a strong deviation from a linear composition dependence, as is common for III–V semiconductor alloys.[91] However, our measured slope is so small, even smaller than the calculated slope of the indirect gap, such that it cannot be explained solely by such a non-linearity. Thus, we attribute the deviation to the relaxation of electron momentum conservation during optical transitions as the translational symmetry is increasingly broken by Al atoms occupying random cation sites. Correspondingly, the experimentally observed onset of interband transitions tends towards the fundamental (indirect) bandgap with increasing x, consistent with the data in the inset, showing a continuous transition of the measured E_g from the expected value for the direct transition for x = 0 to approximately the expected value for the indirect transition for x = 0.44. We note that the initial slight decrease in the measured E_g from 2.3 to 2.2 eV with increasing x = 0 to 0.09 is opposite to the expected increasing bandgap and is also opposite to the expected trend based on the Burstein–Moss shift which would cause an increase in the optical gap with increasing N^*. Thus, similar to the argument above, we attribute the decrease from 2.3 to 2.2 eV to the relaxation of the momentum conservation due to the addition of Al, consistent with a decrease in the slope of the measured α *vs.* $\hbar\omega$ curve in Fig. 6 as x is increased from 0 to 0.09.

Conclusions

The presented X-ray diffraction and optical measurement results demonstrate the tunability of the strain and bandgap in rocksalt structure $(Ti_{0.5}Mg_{0.5})_{1-x}Al_xN$ semiconductors. Epitaxial $(Ti_{0.5}Mg_{0.5})_{1-x}Al_xN$(001) layers are deposited on MgO(001) by reactive magnetron co-sputtering at 700 °C. $x \leq 0.44$ yields single phase solid solution alloys but a secondary phase emerges at higher Al content. The crystalline quality of rocksalt $(Ti_{0.5}Mg_{0.5})_{1-x}Al_xN$ increases with increasing $x \leq 0.33$ due to a decreasing lattice mismatch with the substrate, which also results in a decreasing degree of relaxation. Layers with $x \geq 0.22$ are fully strained. The measured relaxed lattice constant follows a linear composition dependence $a_o = (4.269 - 0.131x)$ Å for $x \leq 0.33$ but deviates above this line for x = 0.44. In contrast, density functional theory calculations predict an $a_o = (4.308 - 0.234x)$ Å that is linear over the entire composition range x = 0–1.0 and which has a nearly twice as strong composition dependence than the experimental measurements, suggesting that some of the Al may not incorporate into the lattice during deposition. The optical free carrier density determined from the optical reflection edge increases slightly from 1.4 × 10^{22} cm^{-3} for $Ti_{0.5}Mg_{0.5}N$ (x = 0.00) to 1.5 × 10^{22} cm^{-3} for x = 0.09 but subsequently decreases to 0.93 × 10^{22} cm^{-3} for x = 0.44. This composition dependence is attributed to a decrease in the dislocation density and an increase in the bandgap with increasing x. The latter also results in an increasing carrier localization, as determined from resistivity measurements at 295 and 77 K. First-principles calculations indicate that the fundamental indirect bandgap increases with Al content from 1.0 eV for x = 0 to 2.0 and 2.2 eV for x = 0.25 and 0.50, while the direct gap at x = 0 is 2.1 eV. Optical analyses indicate that the optical bandgap increases only slightly from 2.3 to 2.6 eV for x = 0 to 0.44. The former value is attributed to the onset of direct interband transition in $Ti_{0.5}Mg_{0.5}N$ while the latter is more indicative of the fundamental (indirect) gap in $Ti_{0.28}Mg_{0.28}Al_{0.44}N$ which exhibits strong absorption due to the relaxation of the momentum conservation by the random occupation of cation sites by Al.

Author contributions

The manuscript was written through contributions of all authors. All authors have given approval to the final version of the manuscript.

Conflicts of interest

There are no conflicts to declare.

Acknowledgements

The authors acknowledge financial support by the National Science Foundation under Grant No. 1712752, 1629230, and 1629239. Computational resources were provided by the Center for Computational Innovations at RPI and at the Ohio Supercomputer Center (OSC).[92]

References

1 J. E. Sundgren, Structure and properties of TiN coatings, *Thin Solid Films*, 1985, **128**(1), 21–44.
2 H. Holleck, Material selection for hard coatings, *J. Vac. Sci. Technol., A*, 1986, **4**(6), 2661–2669.
3 L. Hultman, Thermal stability of nitride thin films, *Vacuum*, 2000, **57**(1), 1–30.
4 J. Musil, Hard and superhard nanocomposite coatings, *Surf. Coat. Technol.*, 2000, **125**(1), 322–330.
5 C.-S. Shin, D. Gall, N. Hellgren, J. Patscheider, I. Petrov and J. E. Greene, Vacancy hardening in single-crystal TiN_x(001) layers, *J. Appl. Phys.*, 2003, **93**(10), 6025–6028.
6 J. Westlinder, T. Schram, L. Pantisano, E. Cartier, A. Kerber, G. S. Lujan, J. Olsson and G. Groeseneken, On the thermal stability of atomic layer deposited TiN as gate electrode in MOS devices, *IEEE Electron Device Lett.*, 2003, **24**(9), 550–552.
7 G. V. Naik, V. M. Shalaev and A. Boltasseva, Alternative Plasmonic Materials: Beyond Gold and Silver, *Adv. Mater.*, 2013, **25**(24), 3264–3294.
8 K. Balasubramanian, S. V. Khare and D. Gall, Valence electron concentration as an indicator for mechanical properties in rocksalt structure nitrides, carbides and carbonitrides, *Acta Mater.*, 2018, **152**, 175–185.
9 B. Saha, J. A. Perez-Taborda, J.-H. Bahk, Y. R. Koh, A. Shakouri, M. Martin-Gonzalez and T. D. Sands, Temperature-dependent thermal and thermoelectric properties of n-type and p-type $Sc_{1-x}Mg_xN$, *Phys. Rev. B*, 2018, **97**(8), 085301.
10 M. A. Gharavi, R. Armiento, B. Alling and P. Eklund, Theoretical study of phase stability, crystal and electronic structure of $MeMgN_2$ (Me = Ti, Zr, Hf) compounds, *J. Mater. Sci.*, 2018, **53**, 4294–4305.
11 N. Tureson, M. Marteau, T. Cabioch, N. Van Nong, J. Jensen, J. Lu, G. Greczynski, D. Fournier, N. Singh, A. Soni, L. Belliard, P. Eklund and A. le Febvrier, Effect of ion-implantation-induced defects and Mg dopants on the thermoelectric properties of ScN, *Phys. Rev. B*, 2018, **98**(20), 205307.
12 P. Patsalas, N. Kalfagiannis, S. Kassavetis, G. Abadias, D. V. Bellas, C. Lekka and E. Lidorikis, Conductive nitrides: Growth principles, optical and electronic properties, and their perspectives in photonics and plasmonics, *Mater. Sci. Eng., R*, 2018, **123**, 1–55.
13 C. Metaxa, S. Kassavetis, J. F. Pierson, D. Gall and P. Patsalas, Infrared Plasmonics with Conductive Ternary Nitrides, *ACS Appl. Mater. Interfaces*, 2017, **9**(12), 10825–10834.
14 P. Patsalas, N. Kalfagiannis and S. Kassavetis, Optical Properties and Plasmonic Performance of Titanium Nitride, *Materials*, 2015, **8**(6), 3128.
15 M. Garbrecht, L. Hultman, M. H. Fawey, T. D. Sands and B. Saha, Tailoring of surface plasmon resonances in TiN/$(Al_{0.72}Sc_{0.28})N$ multilayers by dielectric layer thickness variation, *J. Mater. Sci.*, 2018, **53**(6), 4001–4009.
16 S. Kassavetis, A. Hodroj, C. Metaxa, S. Logothetidis, J. F. Pierson and P. Patsalas, Optical and electronic properties of conductive ternary nitrides with rare- or alkaline-earth elements, *J. Appl. Phys.*, 2016, **120**(22), 225106.
17 B. Saha, G. V. Naik, S. Saber, C. Akatay, E. A. Stach, V. M. Shalaev, A. Boltasseva and T. D. Sands, TiN/(Al,Sc)N metal/dielectric superlattices and multilayers as hyperbolic metamaterials in the visible spectral range, *Phys. Rev. B: Condens. Matter Mater. Phys.*, 2014, **90**(12), 125420.
18 P. Eklund, S. Kerdsongpanya and B. Alling, Transition-metal-nitride-based thin films as novel energy harvesting materials, *J. Mater. Chem. C*, 2016, **4**(18), 3905–3914.
19 B. Alling, Metal to semiconductor transition and phase stability of $Ti_{1-x}Mg_xN_y$ alloys investigated by first-principles calculations, *Phys. Rev. B: Condens. Matter Mater. Phys.*, 2014, **89**(8), 085112.
20 R. Deng, B. D. Ozsdolay, P. Y. Zheng, S. V. Khare and D. Gall, Optical and transport measurement and first-principles determination of the ScN band gap, *Phys. Rev. B: Condens. Matter Mater. Phys.*, 2015, **91**(4), 045104.
21 R. Deng, P. Y. Zheng and D. Gall, Optical and electron transport properties of rock-salt $Sc_{1-x}Al_xN$, *J. Appl. Phys.*, 2015, **118**(1), 015706.
22 S. Kerdsongpanya, B. Alling and P. Eklund, Phase stability of ScN-based solid solutions for thermoelectric applications from first-principles calculations, *J. Appl. Phys.*, 2013, **114**(7), 073512.
23 B. Biswas and B. Saha, Development of semiconducting ScN, *Phys. Rev. Mater.*, 2019, **3**(2), 020301.
24 S. R. Bauers, A. Holder, W. Sun, C. L. Melamed, R. Woods-Robinson, J. Mangum, J. Perkins, W. Tumas, B. Gorman, A. Tamboli, G. Ceder, S. Lany and A. Zakutayev, Ternary nitride semiconductors in the rocksalt crystal structure, *Proc. Natl. Acad. Sci. U. S. A.*, 2019, 201904926.
25 S. R. Bauers, J. Mangum, S. P. Harvey, J. D. Perkins, B. Gorman and A. Zakutayev, Epitaxial growth of rock salt $MgZrN_2$ semiconductors on MgO and GaN, *Appl. Phys. Lett.*, 2020, **116**(10), 102102.
26 B. Wang, S. Kerdsongpanya, M. E. McGahay, E. Milosevic, P. Patsalas and D. Gall, Growth and properties of epitaxial $Ti_{1-x}Mg_xN$(001) layers, *J. Vac. Sci. Technol., A*, 2018, **36**(6), 061501.
27 B. Wang and D. Gall, In A new semiconductor: $Ti_{0.5}Mg_{0.5}$-N(001), 2018 IEEE Nanotechnology Symposium (ANTS), 14–15 Nov. 2018, IEEE, 2018; pp. 1–5.
28 H. Hoche, J. Schmidt, S. Groß, T. Troßmann and C. Berger, PVD coating and substrate pretreatment concepts for corrosion and wear protection of magnesium alloys, *Surf. Coat. Technol.*, 2011, **205**, S145–S150.
29 H. Hoche, S. Groß, R. Foerster, J. Schmidt and W. Adamitzki, Development of Decorative and Corrosion Resistant Coatings

for the Surface Refinement of Magnesium Alloys by Plasma-based Methods, *Plasma Processes Polym.*, 2009, **6**(S1), S671–S677.
30 K. Balasubramanian, S. V. Khare and D. Gall, Energetics of point defects in rocksalt structure transition metal nitrides: Thermodynamic reasons for deviations from stoichiometry, *Acta Mater.*, 2018, **159**, 77–88.
31 B. Wang and D. Gall, Fully strained epitaxial $Ti_{1-x}Mg_xN$-(001) layers, *Thin Solid Films*, 2019, **688**, 137165.
32 E. Milosevic, S. Kerdsongpanya, M. E. McGahay, B. Wang and D. Gall, The Resistivity Size Effect in Epitaxial Nb(001) and Nb(011) Layers, *IEEE Trans. Electron Devices*, 2019, **66**(8), 3473–3478.
33 M. E. McGahay and D. Gall, Conductive surface oxide on CrN(001) layers, *Appl. Phys. Lett.*, 2019, **114**(13), 131602.
34 R. T. Haasch, T.-Y. Lee, D. Gall, J. E. Greene and I. Petrov, Epitaxial TiN(001) Grown and Analyzed In situ by XPS and UPS. II. Analysis of Ar^+ Sputter Etched Layers, *Surf. Sci. Spectra*, 2000, **7**(3), 204–212.
35 N. Finnegan, R. T. Haasch, D. Gall, S. Kodambaka, J. E. Greene and I. Petrov, A Comparison of Auger Electron Spectra from Stoichiometric Epitaxial TiN(001) After (1) UHV Cleaving and (2) Ar^+ Sputter Etching, *Surf. Sci. Spectra*, 2000, **7**(2), 93–100.
36 E. D. Palik, *Handbook of optical constants of solids II*. Academic press, Boston, 1991, p. 950.
37 O. S. Heavens, *Optical properties of thin solid films*, Courier Corporation North Chelmsford, MA, 1991.
38 D. Gall, I. Petrov and J. E. Greene, Epitaxial $Sc_{1-x}Ti_xN(001)$: Optical and electronic transport properties, *J. Appl. Phys.*, 2001, **89**(1), 401–409.
39 G. Kresse and J. Furthmüller, Efficient iterative schemes for ab initio total-energy calculations using a plane-wave basis set, *Phys. Rev. B: Condens. Matter Mater. Phys.*, 1996, **54**(16), 11169–11186.
40 P. E. Blöchl, Projector augmented-wave method, *Phys. Rev. B: Condens. Matter Mater. Phys.*, 1994, **50**(24), 17953–17979.
41 G. Kresse and D. Joubert, From ultrasoft pseudopotentials to the projector augmented-wave method, *Phys. Rev. B: Condens. Matter Mater. Phys.*, 1999, **59**(3), 1758–1775.
42 J. P. Perdew, K. Burke and M. Ernzerhof, Generalized Gradient Approximation Made Simple, *Phys. Rev. Lett.*, 1996, **77**(18), 3865–3868.
43 A. van de Walle, P. Tiwary, M. de Jong, D. L. Olmsted, M. Asta, A. Dick, D. Shin, Y. Wang, L. Q. Chen and Z. K. Liu, Efficient stochastic generation of special quasirandom structures, *CALPHAD: Comput. Coupling Phase Diagrams Thermochem.*, 2013, **42**, 13–18.
44 S. H. Wei, L. G. Ferreira, J. E. Bernard and A. Zunger, Electronic properties of random alloys: Special quasirandom structures, *Phys. Rev. B: Condens. Matter Mater. Phys.*, 1990, **42**(15), 9622–9649.
45 A. Zunger, S. H. Wei, L. G. Ferreira and J. E. Bernard, Special quasirandom structures, *Phys. Rev. Lett.*, 1990, **65**(3), 353–356.
46 V. Adhikari, N. J. Szymanski, I. Khatri, D. Gall and S. V. Khare, First principles investigation into the phase stability and enhanced hardness of TiN–ScN and TiN–YN alloys, *Thin Solid Films*, 2019, **688**, 137284.
47 Z. T. Y. Liu, B. P. Burton, S. V. Khare and D. Gall, First-principles phase diagram calculations for the rocksalt-structure quasibinary systems TiN–ZrN, TiN–HfN and ZrN–HfN, *J. Phys.: Condens. Matter*, 2016, **29**(3), 035401.
48 J. Heyd, G. E. Scuseria and M. Ernzerhof, Hybrid functionals based on a screened Coulomb potential, *J. Chem. Phys.*, 2003, **118**(18), 8207–8215.
49 F. Moens, S. Konstantinidis and D. Depla, The Target Material Influence on the Current Pulse during High Power Pulsed Magnetron Sputtering, *Front. Phys.*, 2017, **5**, 51.
50 P.-A. Cormier, A. Balhamri, A.-L. Thomann, R. Dussart, N. Semmar, J. Mathias, R. Snyders and S. Konstantinidis, Measuring the energy flux at the substrate position during magnetron sputter deposition processes, *J. Appl. Phys.*, 2013, **113**(1), 013305.
51 D. K. Smith and H. R. Leider, Low-temperature thermal expansion of LiH, MgO and CaO, *J. Appl. Crystallogr.*, 1968, **1**(4), 246–249.
52 M. Fenker, M. Balzer, H. Kappl and O. Banakh, Some properties of (Ti,Mg)N thin films deposited by reactive dc magnetron sputtering, *Surf. Coat. Technol.*, 2005, **200**(1–4), 227–231.
53 H. Vollstädt, E. Ito, M. Akaishi, S. Akimoto and O. Fukunaga, High Pressure Synthesis of Rocksalt Type of AlN, *Proc. Jpn. Acad., Ser. B*, 1990, **66**(1), 7–9.
54 P. Zheng, B. D. Ozsdolay and D. Gall, Epitaxial growth of tungsten layers on MgO(001), *J. Vac. Sci. Technol., A*, 2015, **33**(6), 061505.
55 G. Greczynski, J. Lu, J. Jensen, S. Bolz, W. Kölker, C. Schiffers, O. Lemmer, J. E. Greene and L. Hultman, A review of metal-ion-flux-controlled growth of metastable TiAlN by HIPIMS/DCMS co-sputtering, *Surf. Coat. Technol.*, 2014, **257**, 15–25.
56 K. Zhang, K. Balasubramanian, B. D. Ozsdolay, C. P. Mulligan, S. V. Khare, W. T. Zheng and D. Gall, Growth and mechanical properties of epitaxial NbN(001) films on MgO(001), *Surf. Coat. Technol.*, 2016, **288**, 105–114.
57 B. D. Ozsdolay, C. P. Mulligan, M. Guerette, L. Huang and D. Gall, Epitaxial growth and properties of cubic WN on MgO(001), MgO(111), and Al_2O_3(0001), *Thin Solid Films*, 2015, **590**, 276–283.
58 B. D. Ozsdolay, X. Shen, K. Balasubramanian, G. Scannell, L. Huang, M. Yamaguchi and D. Gall, Elastic constants of epitaxial cubic MoN_x(001) layers, *Surf. Coat. Technol.*, 2017, **325**, 572–578.
59 D. Gall, C.-S. Shin, R. T. Haasch, I. Petrov and J. E. Greene, Band gap in epitaxial NaCl-structure CrN(001) layers, *J. Appl. Phys.*, 2002, **91**(9), 5882–5886.
60 C.-S. Shin, D. Gall, Y.-W. Kim, P. Desjardins, I. Petrov, J. E. Greene, M. Odén and L. Hultman, Epitaxial NaCl structure δ-TaN_x(001): Electronic transport properties, elastic modulus, and hardness *versus* N/Ta ratio, *J. Appl. Phys.*, 2001, **90**(6), 2879–2885.
61 D. Gall, I. Petrov, P. Desjardins and J. E. Greene, Microstructural evolution and Poisson ratio of epitaxial ScN grown on TiN(001)/MgO(001) by ultrahigh vacuum reactive magnetron sputter deposition, *J. Appl. Phys.*, 1999, **86**(10), 5524–5529.
62 A. B. Mei, M. Tuteja, D. G. Sangiovanni, R. T. Haasch, A. Rockett, L. Hultman, I. Petrov and J. E. Greene, Growth,

nanostructure, and optical properties of epitaxial VN_x/MgO(001) (0.80 [less-than-or-equal] × [less-than-or-equal] 1.00) layers deposited by reactive magnetron sputtering, *J. Mater. Chem. C*, 2016, **4**(34), 7924–7938.

63 C.-S. Shin, S. Rudenja, D. Gall, N. Hellgren, T.-Y. Lee, I. Petrov and J. E. Greene, Growth, surface morphology, and electrical resistivity of fully strained substoichiometric epitaxial TiN_x ($0.67 \leqslant x < 1.0$) layers on MgO(001), *J. Appl. Phys.*, 2004, **95**(1), 356–362.

64 K. Zhang, M. Wen, S. Wang, R. P. Deng, D. Gall and W. T. Zheng, Sputter deposited NbC_xN_y films: Effect of nitrogen content on structure and mechanical and tribological properties, *Surf. Coat. Technol.*, 2014, **258**, 746–753.

65 R. K. Choudhary, P. Mishra and R. C. Hubli, Deposition of rock salt AlN coatings by magnetron sputtering, *Surf. Eng.*, 2014, **30**(8), 535–539.

66 A. Madan, I. W. Kim, S. C. Cheng, P. Yashar, V. P. Dravid and S. A. Barnett, Stabilization of Cubic AlN in Epitaxial AlN/TiN Superlattices, *Phys. Rev. Lett.*, 1997, **78**(9), 1743–1746.

67 I. Yoshihiro and U. Mamoru, First-principles calculations of semiconducting $TiMgN_2$, *Jpn. J. Appl. Phys.*, 2016, **55**(9), 098001.

68 H. Berkok, A. Tebboune, A. Saim and A. H. Belbachir, Structural and electronic properties of $Sc_xAl_{1-x}N$: First principles study, *Phys. B*, 2013, **411**, 1–6.

69 Y. C. Cheng, X. L. Wu, J. Zhu, L. L. Xu, S. H. Li and P. K. Chu, Optical properties of rocksalt and zinc blende AlN phases: First-principles calculations, *J. Appl. Phys.*, 2008, **103**(7), 073707.

70 J. Paier, M. Marsman, K. Hummer, G. Kresse, I. C. Gerber and J. G. Ángyán, Screened hybrid density functionals applied to solids, *J. Chem. Phys.*, 2006, **124**(15), 154709.

71 J. L. Endrino, C. Århammar, A. Gutiérrez, R. Gago, D. Horwat, L. Soriano, G. Fox-Rabinovich, D. Martín y Marero, J. Guo, J. E. Rubensson and J. Andersson, Spectral evidence of spinodal decomposition, phase transformation and molecular nitrogen formation in supersaturated TiAlN films upon annealing, *Acta Mater.*, 2011, **59**(16), 6287–6296.

72 R. Deng, S. R. Evans and D. Gall, Bandgap in $Al_{(1-x)}Sc_xN$, *Appl. Phys. Lett.*, 2013, **102**(11), 112103.

73 S. R. Bauers, D. M. Hamann, A. Patterson, J. D. Perkins, K. R. Talley and A. Zakutayev, Composition, structure, and semiconducting properties of $Mg_xZr_{2-x}N_2$ thin films, *Jpn. J. Appl. Phys.*, 2019, **58**(SC), SC1015.

74 M. E. McGahay, B. Wang, J. Shi and D. Gall, Band gap and electron transport in epitaxial cubic $Cr_{1-x}Al_xN$(001), *Phys. Rev. B*, 2020, **101**(20), 205206.

75 A. Hodroj, O. Chaix-Pluchery, P. Steyer and J. F. Pierson, Oxidation resistance of decorative (Ti,Mg)N coatings deposited by hybrid cathodic arc evaporation-magnetron sputtering process, *Surf. Coat. Technol.*, 2011, **205**(19), 4547–4553.

76 M. Fenker, M. Balzer and H. Kappl, Corrosion behaviour of decorative and wear resistant coatings on steel deposited by reactive magnetron sputtering – Tests and improvements, *Thin Solid Films*, 2006, **515**(1), 27–32.

77 X. Y. Zhang, J. S. Chawla, B. M. Howe and D. Gall, Variable-range hopping conduction in epitaxial CrN(001), *Phys. Rev. B: Condens. Matter Mater. Phys.*, 2011, **83**(16), 165205.

78 J. Jiang, X. Sun, X. Chen, B. Wang, Z. Chen, Y. Hu, Y. Guo, L. Zhang, Y. Ma, L. Gao, F. Zheng, L. Jin, M. Chen, Z. Ma, Y. Zhou, N. P. Padture, K. Beach, H. Terrones, Y. Shi, D. Gall, T.-M. Lu, E. Wertz, J. Feng and J. Shi, Carrier lifetime enhancement in halide perovskite via remote epitaxy, *Nat. Commun.*, 2019, **10**(1), 4145.

79 X. Y. Zhang, J. S. Chawla, R. P. Deng and D. Gall, Epitaxial suppression of the metal-insulator transition in CrN, *Phys. Rev. B: Condens. Matter Mater. Phys.*, 2011, **84**(7), 073101.

80 B. D. Ozsdolay, C. P. Mulligan, K. Balasubramanian, L. Huang, S. V. Khare and D. Gall, Cubic β-WN_x layers: Growth and properties *vs.* N-to-W ratio, *Surf. Coat. Technol.*, 2016, **304**, 98–107.

81 C.-S. Shin, D. Gall, P. Desjardins, A. Vailionis, H. Kim, I. Petrov, J. E. Greene and M. Odén, Growth and physical properties of epitaxial metastable cubic TaN(001), *Appl. Phys. Lett.*, 1999, **75**(24), 3808–3810.

82 H.-S. Seo, T.-Y. Lee, I. Petrov, J. E. Greene and D. Gall, Epitaxial and polycrystalline HfN_x (0.8 × 1.5) layers on MgO(001): Film growth and physical properties, *J. Appl. Phys.*, 2005, **97**(8), 083521.

83 F. Tian, J. D'Arcy-Gall, T.-Y. Lee, M. Sardela, D. Gall, I. Petrov and J. E. Greene, Epitaxial $Ti_{1-x}W_xN$ alloys grown on MgO(001) by ultrahigh vacuum reactive magnetron sputtering: Electronic properties and long-range cation ordering, *J. Vac. Sci. Technol., A*, 2003, **21**(1), 140–146.

84 C. E. Lekka, P. Patsalas, P. Komninou and G. A. Evangelakis, Electronic properties and bonding characteristics of AlN:Ag thin film nanocomposites, *J. Appl. Phys.*, 2011, **109**(5), 054310.

85 N. Pliatsikas, A. Siozios, S. Kassavetis, G. Vourlias and P. Patsalas, Optical properties of nanostructured Al-rich $Al_{1-x}Ti_xN$ films, *Surf. Coat. Technol.*, 2014, **257**, 63–69.

86 D. y. Wang, Y. Nagahata, M. Masuda and Y. Hayashi, Effect of nonstoichiometry upon optical properties of radio frequency sputtered Al–N thin films formed at various sputtering pressures, *J. Vac. Sci. Technol., A*, 1996, **14**(6), 3092–3099.

87 H. Yamashita, K. Fukui, S. Misawa and S. Yoshida, Optical properties of AlN epitaxial thin films in the vacuum ultraviolet region, *J. Appl. Phys.*, 1979, **50**(2), 896–898.

88 B. Wang, K. Aryana, J. T. Gaskins, P. E. Hopkins, S. V. Khare and D. Gall, Structural Stabilization and Piezoelectric Enhancement in Epitaxial $(Ti_{1-x}Mg_x)_{0.25}Al_{0.75}N$(0001) Layers, *Adv. Funct. Mater.*, 2020, **30**(23), 2001915.

89 B. Saha, S. Saber, G. V. Naik, A. Boltasseva, E. A. Stach, E. P. Kvam and T. D. Sands, Development of epitaxial $Al_xSc_{1-x}N$ for artificially structured metal/semiconductor superlattice metamaterials, *Phys. Status Solidi B*, 2015, **252**(2), 251–259.

90 Z.-Y. Jiao, S.-H. Ma and J.-F. Yang, A comparison of the electronic and optical properties of zinc blende, rocksalt and wurtzite AlN: A DFT study, *Solid State Sci.*, 2011, **13**(2), 331–336.

91 I. Gorczyca, T. Suski, N. E. Christensen and A. Svane, Band gap bowing in quaternary nitride semiconducting alloys, *Appl. Phys. Lett.*, 2011, **98**(24), 241905.

92 Ohio supercomputer center. 1987, http://osc.edu/ark:/19495/f5s1ph73.

